Wireless Electromagnetic Sensors for Image-Guided Cardiothoracic Procedures

Daragh Crowley, *Member, IEEE*, Marco Cavaliere, *Member, IEEE*, Eoin Higgins, *Member, IEEE*, Charu Pande, *Member, IEEE*, Herman Alexander Jaeger, *Member, IEEE*, Kilian O'Donoghue, and Pádraig Cantillon-Murphy, *Senior Member, IEEE*

***Abstract*—Electromagnetic tracking (EMT) is essential in surgical navigation without line of sight and to reduce the use of harmful radiation-based imaging. The inductive sensors used in current EMT systems are small, often less than a millimeter in diameter, but the need for a wired connection from the sensor to the control unit can cause obstructions and complicate the surgical field. This work introduces a novel wireless method of tracking electromagnetic (EM) sensors with immediate applications intended to streamline surgical workflows. Wireless EM 6-degree-of-freedom (DOF) sensor nodes were designed and manufactured with the intended use as a patient-mounted registration device. The battery-powered prototype device was shown to have a position and orientation trueness of 0.84 mm and 0.7°, respectively, over a tracking volume of 40 × 40 × 35 cm. The sensor node performs analog and digital signal processing and uses bluetooth low energy (BLE) to transmit the sensor data at a 25-Hz refresh rate. The Bluetooth-based wireless EM sensor nodes developed in this work have comparable performance to standard wired sensors and were tested in both a static volume characterization and a dynamic ex vivo lung model. The work in this article is based on the open-source Anser EMT system although the approach can be generalized to any tracking system. Wireless EMT offers the potential to introduce computer-assisted navigation in surgical procedures where wired sensors were previously infeasible.**

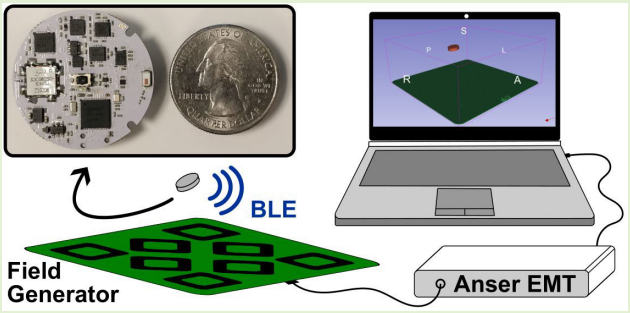

***Index Terms*— Bluetooth, electromagnetic tracking (EMT), endoscopy, image-guided surgery, localization, navigation, wearable sensors, wireless sensor networks.**

I. Introduction

ELECTROMAGNETIC tracking (EMT) has been widely used in both research and clinical settings for enhancing image-guided surgical interventions without requiring line of sight and avoiding increased use of ionizing-radiation-based imaging [1]. A spatially varying magnetic field is created by a field generator usually placed near or beneath the patient on the operating table. Miniature inductive coil sensors, typically less than a millimeter in diameter, measure the field as a small induced voltage, which is then sampled and processed to determine the sensor position and orientation with millimeter- and degree-scale accuracy [2]. The requirement for an extra wire for each sensor to be tracked adds complexity to the operating space, hindering the movement of surgical staff around the patient and negatively affecting device usability [3].

This work focuses on cardiothoracic interventions where EMT is of benefit including cardiac electrophysiology (EP) mapping [4] and flexible bronchoscopy [5], [6]. Accurate real-time registration of the patient's anatomy to preoperative images used for navigation is crucial for the successful outcome of these procedures [7].

Until recently, EP mapping has required intensive X-ray exposure for the patient and clinician. However, magnetic navigation has transformed EP mapping over the past decade by combining position sensing, which does not require X-ray exposure with existing EP mapping techniques, providing clinicians with highly localized position information for diagnosis and treatment. Magnetic navigation has reduced radiation exposure in EP mapping procedures by combining tiny sensors inside the instrument with patient-mounted sensors (see

Received 27 June 2024; revised 20 August 2024; accepted 20 August 2024. Date of publication 19 September 2024; date of current version 14 November 2024. This work was supported in part by the Science Foundation Ireland under Grant 17/CDA/4771 and Grant TIDA17/4897 and in part by the European Union European Research Council (ERC)-2020-Consolidator Grant (COG) under Award 101002225. The associate editor coordinating the review of this article and approving it for publication was Prof. Bin Gao. *(Corresponding author: Daragh Crowley.)*

Daragh Crowley, Marco Cavaliere, Eoin Higgins, Charu Pande, Herman Alexander Jaeger, and Padraig Cantillon-Murphy are with the School of Engineering and the Tyndall National Institute, University College Cork, T12 HW58 Cork, Ireland (e-mail: daragh.crowley@tyndall.ie).

Kilian O'Donoghue is with Quadrant Scientific Ltd., T12 Y275 Cork, Ireland.

Digital Object Identifier 10.1109/JSEN.2024.3458454

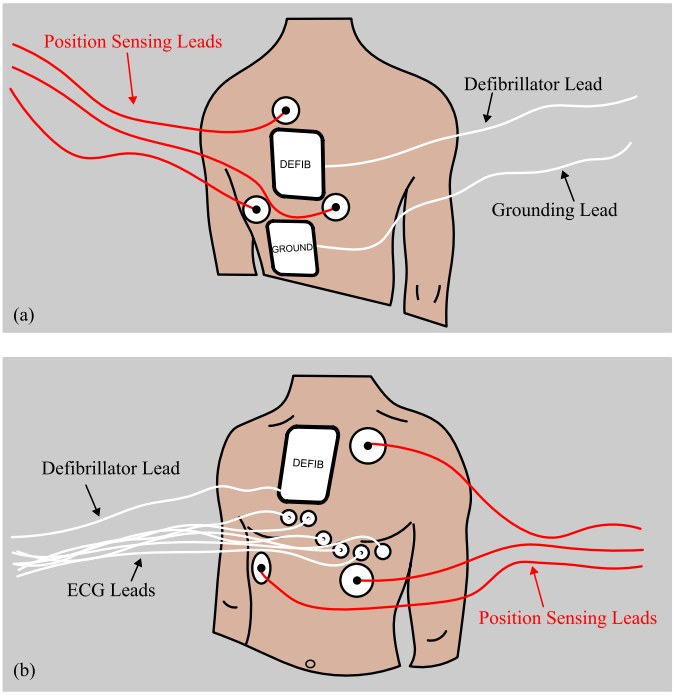

Fig. 1. Patient sensing patches required during EP mapping procedures include defibrillator and ECG electrodes along with EM position reference sensors. (a) Back of patient. (b) Front of patient.

Fig. 1). However, this requires up to six additional wired sensors [8] connected to the patient in order to monitor the patient position. This is in addition to the existing defibrillator, grounding, and ECG leads required for the patient. Additional position sensors on the patient would yield even more accurate sensing and potentially better clinical outcomes [8]. However, this is practically impossible due to the existing "rat's nest" of leads already connected to the patient.

The CARTO mapping system (*Biosense Webster, Irvine, CA, USA*) uses EMT to generate a 3-D geometry of the heart's electrical signals for arrhythmia mapping. A wired anatomical reference patch is placed on the patient's back to remove patient movement artifacts during the mapping procedure [9], [10]. The position of the EP mapping catheter is continuously calculated relative to the anatomical reference patch to ensure accurate modeling of the chamber geometry and ablation locations.

Commercially available electromagnetic (EM) navigation bronchoscopy systems including the SPiN Thoracic Navigation System (*Olympus Corporation, Tokyo, Japan*) and superDimension Navigation System (*Medtronic, MN, USA*) also use secondary EM reference sensors attached to the patient's chest during the procedure for anatomical alignment and respiratory gating. Three sensor pads are attached to the chest before the preoperative current transformer (CT), which are then automatically detected in the CT image during the planning stage. When the procedure is ready to begin, the sensors are connected with wires to the control unit.

In this work, a wireless EM sensor tracking system is introduced based on the open-source Anser EMT research platform [11] with prototype sensors tested both in static tracking volume characterization and in a dynamic ex vivo lung model simulator. The developed sensor nodes are designed for use as wireless chest-mounted reference sensors.

A. Electromagnetic Tracking

The wireless tracking system presented here is based on the open-source Anser EMT system previously developed at University College Cork [11]. The main system components are the field generator, control unit, and sensor coils. Frequency-division multiplexing is used to create temporally and spatially varying magnetic fields at eight different frequencies using eight transmitting coils in the field generator. This magnetic field induces a time-varying differential voltage across the inductive sensor coil that is dependent on the sensor position and orientation (pose) in the tracking volume. The magnitude of each frequency component in the signal is proportional to the relative distance between the sensor coil and the respective transmitting coil. Calculating the discrete Fourier transform (DFT) of the sampled sensor voltage gives the amplitude of the magnetic field at different frequencies. The demodulated magnitudes can then be used to solve for the sensor pose using a nonlinear least-squares solver. The solver uses the Levenberg–Marquardt algorithm [12] to minimize the error between the measured values and an analytical model of the magnetic field.

In the standard wired system setup, the control unit synchronously samples the current through the transmitter coils along with the sensor signal. The phase of the sensor voltage signal with respect to the transmitter coil current signal is $\pm\pi/2$ after calibrating the phase effect of the acquisition channels, in the absence of metallic distorters [13]. This phase information is necessary for solving the pose of a single uniaxial sensor. In the wireless case, this phase reference is not readily available as field generation and sensor sampling is based on two different clock sources. Section II-B describes a novel method for synchronizing the analog-to-digital converter (ADC) sampling of multiple devices connected on a bluetooth low energy (BLE) network to the order of microseconds.

B. Related Works

There has been significant interest in achieving a wireless EMT system in recent years but much of the focus has been on integrated circuit (IC) solutions. IC-based wireless EMT solutions, such as those described in the following, tend to require custom, high-power magnetic field driver circuits. This, along with the barrier presented by manufacturing custom IC designs, may potentially limit their use by others in the research field. We sought to create a wireless EMT solution compatible with the previously reported open-source Anser EMT system and achievable with off-the-shelf components to enable easy adoption and design modification by other research groups. To the best of authors' knowledge, the only wireless sensor tracking system based on discrete components was developed by Park et al. [14]. Frequency-division multiplexing with three transmitter frequency components was used. The sampled sensor signal is demodulated using the DFT, and the field magnitudes are transmitted over Bluetooth to the base station. The system avoids the need for signal phase measurement as the 5-degree-of-freedom (DOF) pose can be solved when the three orthogonal field components are measured together. However, requiring a triaxial sensor coil would hinder

further miniaturization or integration of the sensor in a catheter tip.

A number of IC solutions have been developed to achieve wireless sensor tracking. Monge et al. [15] developed a wireless 2-D localization system inspired by nuclear magnetic resonance using an IC designed to shift its transmitter output frequency based on the magnetic field applied to it. The tracking volume (less than 2 cm) was not suitable for many clinical applications, and the large required magnetic field (100-mT scale) may pose a safety risk when used near magnetic objects.

Sharma et al. [16] designed a 3-D localization IC also based on measuring dc magnetic field gradients that used an off-chip Hall-effect sensor to directly measure the field and digitally transmit the field value wirelessly, achieving 100-μm localization resolution. The 7-Hz sampling rate reported is limited by the slow turn-on time of the dc used in the transmitting coils. The sensor was wirelessly powered by a pickup coil wrapped around the outside of the device.

Wireless position tracking is also of use in wireless capsule endoscopy applications to identify the location along the digestive tract where images from the capsule are captured. Jang et al. [17] used an array of eight receiver nodes on the body to receive the signal via body channel communication (BCC) from a four-camera endoscope capsule and estimate its position using contact attenuation compensated-received signal strength indicator technique (CAC-RSSI) with subcentimeter 2-D localization accuracy. The authors carefully characterized the signal attenuation of the phantom used for testing, which may be difficult in real-world applications.

Another method of wirelessly tracking capsule endoscopes is to generate different frequency reference excitation signals using external body-mounted transmitters [18]. The capsule sensor digitizes the received signal and transmits the data wirelessly. Submillimeter 3-DOF position tracking was reported. The magnetic field frequency (2.048 MHZ) used was shown to not be affected by the human body and has the advantage of requiring smaller size and lower power transmit and receive coils. However, the high magnetic field frequency would likely introduce significant eddy currents in nearby metallic conductors, potentially degrading the system usability in the operating room. A similar batteryless localization IC in [19] demonstrated 2-DOF 10-mm position accuracy using a 40.68-MHz transmitter frequency. The medium between the capsule IC and the receiver coils outside the body needs to be characterized, which again may prove difficult in real-world applications.

We previously demonstrated direct frequency modulation of the inductive sensor signal for wireless transmission using an audio transmitter and receiver [20]. The transmitted FM signal was demodulated by the FM receiver connected to the control unit of the Anser EMT system. The reported accuracy of 1.61 mm made it a viable option for accomplishing wireless tracking. However, due to the high power consumption of continuous FM signal transmission, it proved difficult to miniaturize the sensor node as necessary for most target applications, prompting our move to the Bluetooth-based system outlined here.

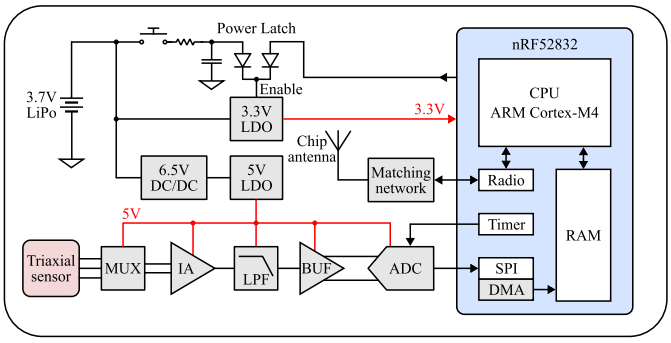

Fig. 2. Sensor block diagram hardware schematic.

A summary of the wireless tracking methods and results of related works.

II. Method

A. Hardware Design

The core component of the wireless sensor node is the nRF52832 Bluetooth 5 system-on-chip (SoC) *(Nordic Semiconductor, Trondheim, Norway)*. The wireless node acquires the sensor signal using an external ADC, demodulates the signal using the DFT, and transmits the demodulated field magnitudes to the base station, which also uses the nRF52832 [21]. An ultrasmall 3.20-mm passive chip antenna and the required matching network are integrated on the printed circuit board (PCB). Fig. 2 outlines the hardware block diagram of the sensor PCB.

The inductive sensor used in this work is a triaxial coil (3DC06ISO-0345J, *Grupo Premo, Málaga, Spain*). The sensor was chosen for its compact size (7 $\times$ 7 mm) with the three sensor coils wound around a single magnetic core. Custom inductive sensor design is also possible based on the requirements of the intended target application [22]. To save PCB space, cost, and power consumption, the three individual sensors are multiplexed before the analog acquisition channel, removing the need for three identical analog signal chains. The 16:2 multiplexer (MAX14661, *Analog Devices, Wilmington, MA, USA*) is capable of switching positive and negative signals from a single supply and has a channel crosstalk of -80 dB, an ON-resistance of 8 Ω, and a 60-MHz bandwidth making it suitable for switching the signal received from the sensor.

The signal induced on the sensor coil is on the order of microvolts and is first amplified with a low noise ($7-\text{nV}/\sqrt{\text{Hz}}$ input voltage noise) instrumentation amplifier (INA821, *Texas Instruments, Dallas, TX, USA*) with gain set to 200. The amplified signal is then filtered using an active two-stage fourth-order Butterworth filter implemented with the AD8617 dual op amp (*Analog Devices*) to remove high frequency noise above 10 kHz [23]. The ADA4941-1 (*Analog Devices*) is used to perform single-ended to differential conversion before sampling with the MAX11198 (*Analog Devices*) 16-bit SAR ADC with the sampling rate set to 100 kHz.

The system is powered by a single 3.7-V, 50-mAh LiPo battery in a 20 $\times$ 10 $\times$ 3.8 mm package. A dc/dc converter boosts the voltage to 6.5 V and two separate low dropout (LDO) regulators provide stable 3.3- and 5-V power rails for

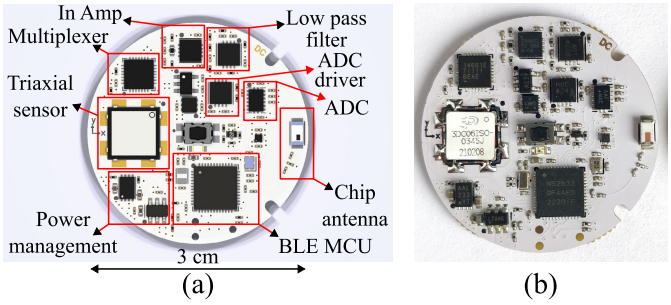

Fig. 3. (a) Rendering of wireless sensor PCB design with main components labeled. (b) Assembled wireless sensor node PCB.

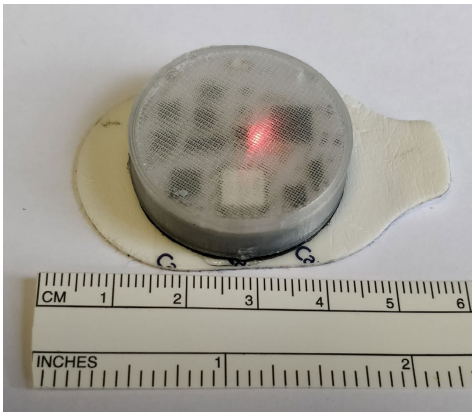

Fig. 4. Wireless patient reference sensor patch prototype. The sensor enclosure is designed to attach to a disposable skin patch allowing the sensors to be reused after the procedure.

the digital and analog components, respectively. The system also includes an integrated battery charge management controller IC (MCP73832, *Microchip Technology, Chandler, AZ, USA*) for easy charging of the devices.

A power latching circuit enables the device to be switched on and off with a small footprint momentary button usually used as a reset button. Pressing the button turns on the 3.3-V LDO long enough for the microcontroller unit (MCU) to initialize and set a general purpose input/output (GPIO) pin high to keep the 3.3-V LDO enabled. After the MCU has set the 3.3-V latch, it can then individually enable the 6.5-V dc/dc converter and 5-V LDO that supplies power to the analog components on the PCB. The button can then be used as a GPIO input for changing device modes or switching off the device.

The PCB was designed with KiCad and manufactured on a circular four-layer FR4 PCB with a diameter of 3 cm. A comparison of the labeled PCB rendering and the assembled device is shown in Fig. 3.

Using a single button rather than a switch for turning on the device allows the PCB and battery to be completely enclosed in a plastic case for sterility and water tightness. The battery can be charged by incorporating a waterproof connector in the enclosure. A plastic enclosure for the PCB and battery was designed and 3-D-printed using flexible polypropylene (PP) filament. The enclosure press-fits to a back cover, 3-D-printed with polylactic acid (PLA) filament. The back cover was super glued to a foam adhesive skin patch. The adhesive skin patch can be disposed of after use and the sensor node enclosure cleaned and sterilized for reuse. Fig. 4 shows a proof-of-concept prototype with the sensor PCB in the 3-D-printed enclosure attached to the adhesive back cover.

B. System Architecture

A custom BLE receiver module was also designed using the nRF52832 microcontroller. It contains an identical analog signal chain and ADC as on the sensor node for sampling the current of the field generator coils. Sampling on the sensor node and receiver module is wirelessly synchronized to provide a direct phase reference between the coil currents and induced sensor voltage.

The programmable peripheral interconnect (PPI) feature of the nRF52832 is used to perform ADC sampling without requiring central processing unit (CPU) intervention. Samples are acquired using a serial peripheral interface (SPI) and stored directly in RAM using direct memory access (EasyDMA). The ADC sampling rate is set at 100 kHz with 2000 samples in each window, leading to a 20-ms window acquisition time.

The Nordic Semiconductor SoftDevice wireless protocol stack is capable of multiple communication protocols including the standard BLE protocol, used in this work for streaming the sensor data, and the proprietary Radio Timeslot API, used here for timer synchronization, which gives the application full control over the radio. The value of a free running timer on the receiver module is broadcast at 30-Hz intervals and is captured by the sensor nodes. The transmission delay is precalibrated and used in resetting the sensor node's timer value to the main timer value. Timer updating is achieved using PPI and low-level software triggers to reduce reliance on the CPU in keeping time synchronization. The synchronized timer automatically triggers the start of a sampling window using PPI.

After 2000 samples are acquired, ADC sampling is paused for 20 ms while the window is processed and wireless transmission takes place, resulting in a total sensor pose refresh rate of 25 Hz. The eight magnetic field magnitude and phase components are placed in a buffer along with the sensor information (device identification (ID) and sensor axis) to be sent to the receiver module in the next available BLE connection event. When the receiver receives the sensor window packet, the sensor voltage phases are corrected by subtracting the phase of the coil currents. The signs of the resulting phases are then applied to the sensor field magnitudes. The signed magnitudes are sent to the PC over a serial connection for sensor pose solving.

The receiver was tested with a simultaneous connection to up to five sensor nodes, limited by the minimum connection interval and transmission time. More sensor nodes can be added at the expense of a refresh rate. In this work, the magnetic field frequencies are set from 2050 to 5900 Hz, spaced by 550 Hz.

C. Device Performance Evaluation

The wireless sensor performance was tested using a two-axis robotic positioning system and an optical tracking system as a gold standard reference (Polaris Vega, *NDI, Waterloo, ON, Canada*) [21]. The sensor was attached to

a custom-made perspex optical tool and placed at varying heights on the robot end-effector. For simplicity, only one of the three sensor axes of the triaxial coil was used in the testing procedure as all three axes share the same analog signal chain and will perform equivalently. The sensor axis tested was directed orthogonally to the surface of the PCB. The robot gantry was mounted on a wooden frame to keep the tracking volume free from metallic distorters.

The sensor was first calibrated by collecting four grids of 5 × 5 points at approximately 15 and 25 cm above the field generator in both the y-orientation (horizontal) and z-orientation (vertical). Calibration scaling factors were found for each of the eight magnetic field components by minimizing the error in a least-squares sense between the sensor measurements and magnetic field model while solving for sensor positions. These scaling factors account for the sensor sensitivity, acquisition channel gain, and DFT processing gain [11].

Test sets were gathered wherein the sensor was repeatedly moved in 30-cm square grids each comprised of 100 points (10 × 10 grids), with the height manually adjusted between each grid to range from 10 to 35 cm above the field generator. The tracking area of the field generator used was 40 × 40 cm; however, the robot positioning system had a span of only 30 cm, limiting the test volume. Grids at each height were collected with the sensor in the field generator x-orientation (horizontal) followed by rotating the sensor and optical tool to the z-orientation (vertical) to give a total of 1200 different sensor poses in the test volume. At each test position, the sensor was held stationary and 50 magnetic measurements were collected for sensor noise and precision analysis. The optical tool position matrices were simultaneously collected. For each grid, the optical positions were fit to the resolved sensor positions by finding a rigid transformation matrix using Horn's absolute orientation method [24] to register the optical position grid to the EM reference frame.

The measurement setup showing the two-axis robotic positioning system and optical tracking system is shown in Fig. 5. The wireless sensor was powered by a 50-mAh LiPo battery during all tests to replicate realistic use. The same testing methodology used for the wireless sensor was repeated for an identical triaxial sensor (3DC06ISO-0345J, *Grupo Premo*) that was connected directly to the Anser base station with shielded twisted-pair wires.

The position error, $\Delta\mathbf{r}(i)$, at the ith test point was defined as the Euclidean distance between the optical tracker position, $\mathbf{r_i} = (x_i, y_i, z_i)$, and the EM sensor position, $\tilde{\mathbf{r}}_\mathbf{i} = (\tilde{x}_i, \tilde{y}_i, \tilde{z}_i)$, solved using the average of the 50 magnetic flux measurements taken at position i as given by the following equation:

$$\Delta\mathbf{r}(i) = \sqrt{(\tilde{x}_i - x_i)^2 + (\tilde{y}_i - y_i)^2 + (\tilde{z}_i - z_i)^2}. \quad (1)$$

The orientation error, $\Delta\mathbf{n}(i)$, was defined as the deviation of the sensor orientation at each location from the mean orientation of each grid where $\mathbf{n}$ and $\bar{\mathbf{n}}$ are the local sensor orientation and mean sensor orientation, respectively,

$$\Delta\mathbf{n}(i) = \frac{180^\circ}{\pi}\left|\cos^{-1}\left(\bar{\mathbf{n}}^\mathrm{T} \cdot \mathbf{n}\right)\right|. \quad (2)$$

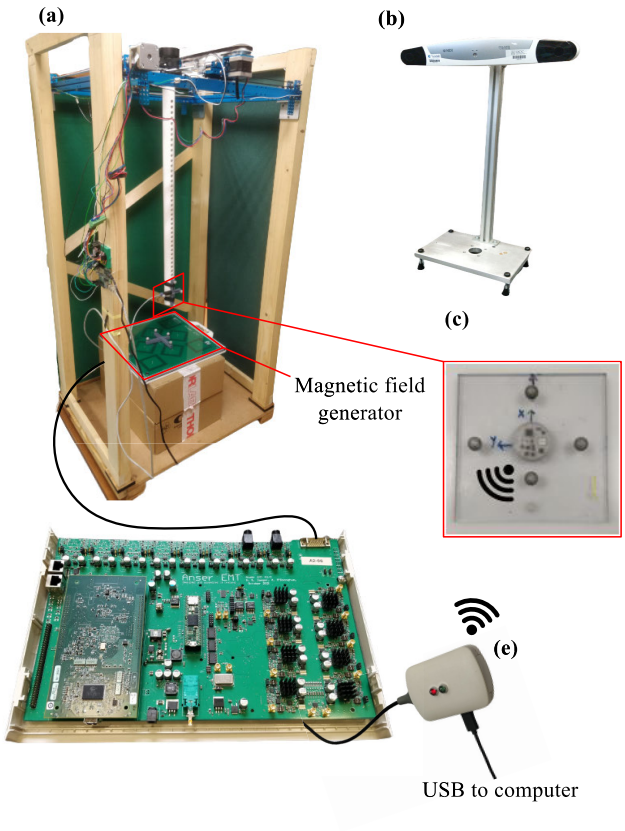

Fig. 5. (a) Two-axis robotic positioning system used for collecting grids of test points with gold standard position measurements provided by (b) NDI Polaris Vega optical tracking system. The wireless EM sensor node was attached to (c) custom optical tool and mounted on the plastic arm of the robot. (d) Anser EMT control unit was connected to the magnetic field generator placed in the robot testing volume. (e) BLE receiver was connected to the control unit to measure the field generator coil currents to obtain a phase reference. The receiver sends the received sensor measurements over a serial connection to the computer running MATLAB for data collection and solving the sensor pose.

The position trueness is defined as the mean error (ME) over all N position or orientation vector, $\mathbf{e}$, in the test volume

$$\mathrm{ME}(\mathbf{e}) = \frac{1}{N}\sum_{i=1}^{N}\mathbf{e_i}. \quad (3)$$

To measure the jitter that would be observed in the sensor position at a stationary point, the precision was calculated from the sensor positions resolved from the 50 flux measurements at each stationary point. The standard deviation over the 50 measurements of the three Cartesian coordinates, σ_x, σ_y, and σ_z, were calculated separately and summed in quadrature to give the local position precision, σ_i, in the following equation:

$$\sigma_i = \sqrt{\sigma_x^2 + \sigma_y^2 + \sigma_z^2}. \quad (4)$$

The global precision, $\bar{\sigma}$, given by the following equation was taken as the mean of all local precision values in the tracked volume:

$$\bar{\sigma} = \frac{1}{N}\sum_{i=1}^{N}\sigma_i. \quad (5)$$

TABLE I
POWER CONSUMPTION ESTIMATE OF SENSOR PCB COMPONENTS

Component	Part number	Power (mW)
ADC	MAX11198	50.63
BLE MCU	nRF52832	26.4
ADC driver	ADA4941	14.67
In Amp	INA821	4.33
Voltage reference	MAX6037	1.4
Multiplexer	MAX14661	0.66
Low pass filter	AD8617	0.27
Total		98.36

D. Ex Vivo Breathing Lung Simulator

To test the wireless sensor nodes in the intended application as a chest-mounted registration and movement compensation sensor, the developed chest patch prototype was applied to the outer wall of a plasticized swine lung model. The lung model was placed in a vacuum chamber with the trachea open to atmospheric pressure and the internal pressure varied to cause the lungs to inflate and deflate with a realistic breathing cycle [25]. The breathing rate was set to 6.34 s with a 50% duty cycle. A CT scan of the inflated lungs was segmented to create a 3-D model of the airways and lung tissue.

MATLAB (Mathworks, Natick, MA, USA) was used to calculate the sensor pose from the wirelessly transmitted magnetic field data and was streamed using IGTLink to Slicer 5.4.0 (https://www.slicer.org) [26] for real-time visualization of the chest sensor position. For demonstration purposes, the lung model was manually registered to the sensor position and the model's position was updated in real time using the data received from the sensor. The sensor position was recorded for 5 min for postprocessing of the respiratory movement data.

III. RESULTS

A. Power Consumption

The estimated power consumption of each component calculated from their respective datasheets is shown in Table I. The microcontroller power consumption depends on the device mode (e.g., ultralow power, BLE advertising or connected, etc.). The estimate in Table I is based on the nRF52832 acting as a BLE peripheral streaming data to a central device at a rate of 2 kB/s. The total current consumption from a 4-V power supply was measured at 25 mA with the sensor node sampling and demodulating the magnetic field and transmitting to the receiver at a rate of 25 Hz. This results in a total power consumption of 100 mW, in line with the estimates from the component datasheets.

When powered with the smallest available lithium polymer battery (3.7 V, 50 mAh, 20 × 10 × 3.8 mm), the battery life of the device in 25-Hz tracking mode was approximately one hour. For procedures requiring longer battery life, a larger battery or lower refresh rate may be used.

B. Phase Synchronization

The timer synchronization method was tested by toggling a GPIO pin at 25 Hz on both the receiver and sensor node and measuring the delay between the signals with an oscilloscope over 5000 periods. The mean and standard deviation of the difference of the toggle time between the receiver and sensor node was 21.72 ± 10.03 μs. The maximum difference was 50 μs over the 5000 measurements.

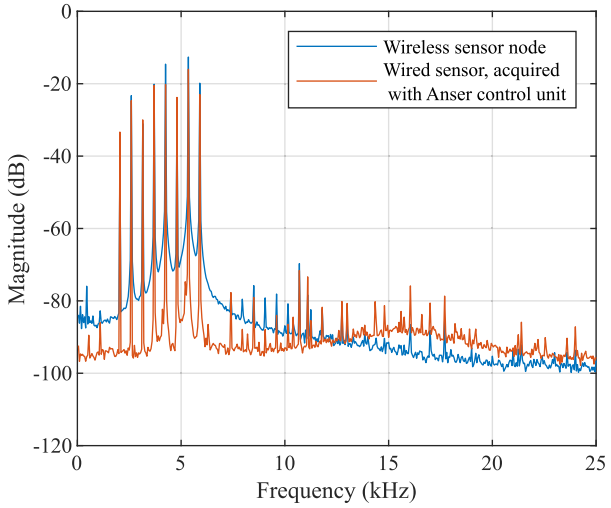

Fig. 6. DFT of the sensor signal acquired with the wireless sensor node and with the Anser control unit. In both cases, the sensor was placed vertically 20 cm above the center of the field generator.

The synchronization accuracy required for stable signal phase measurement is half the period of the maximum magnetic field frequency. For the system setup used in this work, the maximum magnetic field frequency used was 5900 kHz, giving a period of 170 μs. The maximum timer jitter of 50 μs recorded with the oscilloscope test does not cause a sign reversal of the phases.

The sampling synchronization was further tested by placing the sensor in a stationary position above the field generator and recording the sign of the phase difference between the coil current and the sensor voltage. One million phase measurements were recorded over a 16-h duration. The sign of the phase for each field frequency remained consistent for the entire test duration, confirming correct phase synchronization using this method even overextended use.

C. Robot Grid Testing

The spectrum of the fast Fourier transform (FFT) of the sensor signal is shown in Fig. 6, comparing the wireless sensor prototype and the wired sensor acquired using the Anser control unit. Only the amplitudes and phases of the eight frequency components (visible as the eight peaks in the spectrum) are transferred over BLE to reduce the amount of data being transferred. The multiplexing of the sensor input allows the sensor axis to be switched in approximately 1 ms.

The mean position error (accuracy) over the 30 × 30 × 25 cm test volume was 0.84 ± 0.90 mm for the wireless sensor and 0.76 ± 0.65 mm for the case of the comparative wired sensor. The cumulative distribution function of the position errors is shown in Fig. 7.

The mean orientation error was 0.7° for both the wireless and wired sensors.

The precision of the wireless sensor was found to be 1.54 ± 1.50 mm and the wired sensor precision was 0.17 ± 0.13 mm. The wireless sensor precision was less than a millimeter for all grid heights less than 25 cm above the field generator.

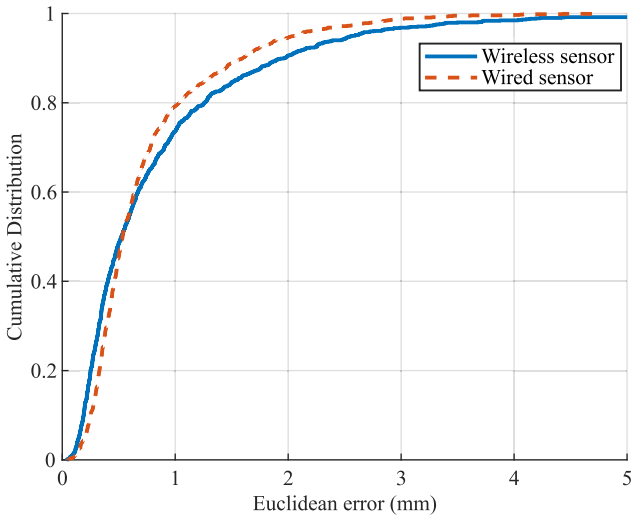

Fig. 7. EMT errors for the wireless sensor prototype device and the wired comparison sensor.

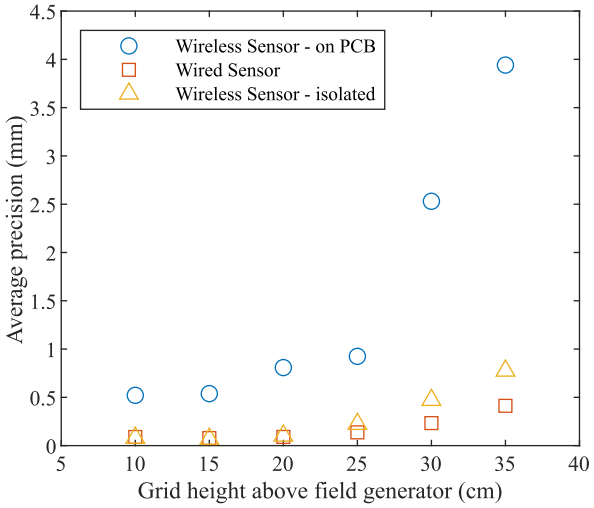

Fig. 8. Sensor position precision measurements for varying grid test heights above the field generator. The wired sensor was connected directly to the Anser EMT control unit for acquisition. Wireless sensor—on PCB and—isolated refers to the sensor placed directly on the wireless PCB prototype and separated from the PCB with a distance greater than 2 cm, respectively.

An increased noise level was observed in the wireless PCB sensor signal which was found to be a result of digital noise from the MCU inducing a voltage on the inductive sensor. Moving the sensor greater than 2 cm away from the MCU was found to mitigate the effect of the noise from the MCU. The test grids described in Section II were repeated with an adapted wireless prototype where the inductive sensor was removed from the PCB and connected with a twisted-pair wire to the PCB to maintain a separation greater than 2 cm during the grid tests. The precision of the wireless sensor with the PCB isolated was 0.29 ± 0.28 mm.

Fig. 8 shows the effect of distance from the field generator on position precision.

D. Dynamic Motion Tracking

The wireless sensor patch was placed on the left lung in a central position, and the resolved sensor poses were recorded at a rate of 25 Hz. The Slicer scene view and recorded motion

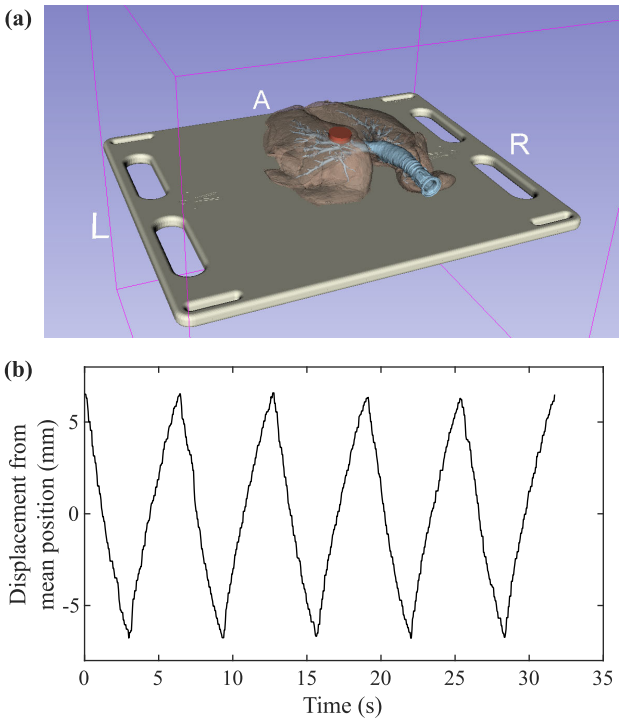

Fig. 9. (a) Slicer scene view with the segmented lung model registered to the wireless sensor node visible in red on the left lung. The field generator model is shown in white beneath the lung model. (b) Breathing motion of the lung recorded using the wireless sensor node.

results are shown in Fig. 9. The respiratory rate observed in the plot matches the pump controller set-point of 6.34 s and 50% duty cycle. The maximal displacement of the lung sensor was 13 mm.

IV. Discussion

Table II shows a comparison of the wireless tracking system developed in this work with other previously developed solutions. It is worth noting that this work differs from most other efforts to develop wireless localization systems in that it was designed using off-the-shelf components on a PCB rather than involving custom IC development. Additionally, the device presented here is compatible with an existing open-source EMT system. The wireless sensor in this work supports the highest sensor tracking rate and is the only wireless tracking system capable of 6-DOF tracking. Using lower frequency magnetic fields will reduce the eddy currents in nearby conductors but the actual distortion caused by this requires further study. Using BLE is convenient as it is widely used and compatible with many devices such as phones, tablets, and computers. However, it may face problems when used in a noisy radio environment such as the operating room if other nearby devices are also using Bluetooth or Wi-Fi.

The main limitation of the sensor node in this work is the power consumption, which is notably higher than the comparable works shown in Table II. The higher power consumption requires a larger battery, limiting the minimum sensor node size achievable. The main source of the higher power consumption is the external ADC used. It was chosen for its high resolution (16 bits), small footprint, and dual simultaneous sampling capability. Future work will seek to

TABLE II
COMPARISON WITH RELATED WIRELESS LOCALIZATION SYSTEMS

Specification	**This work**	[14]	[16]	[18]	[19]	[15]	[17]
Tracking dimension	**6 DOF**	5 DOF	3 DOF	3 DOF	2 DOF	2 DOF	3 DOF
Tracking error	**0.84 mm**	N.R.	0.1 mm	<1 mm	<5 mm	0.5 mm	<1 cm
Angular accuracy	**0.7°**	N.R.	N/A	N/A	N/A	N/A	N/A
Position precision	**0.29 mm**	N.R.	N.R.	N.R.	N.R.	N.R.	N.R.
Refresh rate	**25 Hz**	N.R.	7 Hz	1 Hz	N.R.	N.R.	4 Hz
Power consumption	**100 mW**	N.R.	1 mW[a]	0.336 mW[a]	6 μW [a]	339 μW [a]	1 mW
Sensor size	**30 mm diameter**	38 mm diameter	10.8 × 6.5 mm	26 × 9 mm[b]	12 × 17 mm	1.8 × 1.2 mm[c]	32 × 12 mm
Tracking volume	**40 × 40 × 35 cm**	16 × 16 × 16 cm	20 × 20 × 10 cm	40 × 40 × 40 cm	4 cm	1.2 cm[d]	40 × 60 × 22 cm
Multiple sensors	**Yes**	N.R.	Yes	N.R.	Yes	N.R.	N.R.
Localization modality	**FDM 2-6 kHz**	FDM 17-20 kHz	Magnetic field gradients	FDM 2.048 MHz	Inductive 40.68 MHz	Magnetic field gradients	CAC-RSSI
Wireless protocol	**BLE/Proprietary**	BLE	Backscatter	BFSK	Continuous RF signal	Frequency encoded field	Dual band BCC
Wireless communication frequency	**2.4 GHz**	2.4 GHz	100 kHz	57 MHz	13.56 MHz	500 MHz	40/160 MHz

a IC power only. b Estimate from 000 capsule size. c IC area only. d Tested along single axis. N.R.: Not Reported, N/A: Not Applicable

replace the analog front end and ADC with a lower power IC solution designed for EMT applications such as [27].

The phase synchronization method outlined in this article proved to be robust and well-suited for this application. It requires no changes to the EMT system hardware or field generator. For cases where tracking is required with higher frequency magnetic fields (i.e., for higher update rate), it is possible to further fine-tune the timer synchronization by more accurately calibrating the transmission delay. The main drawback of wireless sensor sampling is the loss of coherent sampling. In the wireless tracking case, the magnetic field signal is generated and sampled based on two separate clocks leading to spectral leakage and scalloping loss. The effect of leakage is clearly visible in Fig. 6 with the signal energy more distributed between the tones in the wireless signal than in the wired case. For the selected frequencies, spectral leakage does not affect accurate amplitude estimation as the tones are spaced far enough apart that crosstalk is negligible. However, scalloping loss due to the frequency of the signal tones falling between two DFT bins will introduce random errors in the amplitude estimation. The effects of scalloping loss can be minimized by using a flat-top window. In this case, there was no significant difference between the flat-top and rectangular windows.

The mean position error over the 30 × 30 × 25 cm test volume was measured to be less than one millimeter, the generally accepted value for use in image-guided interventions [3]. The orientation was only tested for pitch and roll, as yaw may be determined by sampling one of the orthogonal coils on the triaxial sensor. For applications requiring 6-DOF pose tracking, the sensor axis can be selected in software and rapidly switched without negatively impacting the sensor refresh rate. Tracking accuracy may be further improved with further processing of the sensor data such as Kalman filtering [28] or by using evolutionary algorithms [29].

The precision of position measurements is degraded in the case of the wireless sensor node compared with the sensor sampled with the Anser EMT control unit. Wireless precision is degraded by a combination of interference from digital switching in the MCU and the effect of scalloping loss due to the sensed signal frequency not being perfectly coupled with the sampling rate. The position precision is improved from 1.54 to 0.29 mm by separating the inductive sensor from the PCB. Future work will improve the PCB layout to maintain the necessary spacing while still allowing the sensor to be fixed on the PCB. In line with previously published results in [20], the position precision was found to be largely dependent on distance from the field generator, as the signal-to-noise ratio (SNR) degrades with distance from the transmitting coil. This is due to reduced magnetic field strength and induced sensor voltage further from the field generator. A programmable gain amplifier after the instrumentation amplifier could be used to dynamically increase the gain and boost SNR at greater distances from the field generator.

The breathing motion recorded on the breathing lung model is in line with clinical results of pulmonary nodule motion

identified using CT scans [30]. The technology outlined here is highly effective for an automatic registration and breathing motion correction system for use in guided-catheter cardiothoracic procedures as described in [7] and [31].

The wireless tracking system developed in this work was tested in the absence of metallic distorters in a laboratory environment. However, in a clinical setting, there is likely to be many environmental factors to contend with, including metal objects near the tracking volume, temperature fluctuations, and EM interference from other equipment. Further study is required to assess the performance of the wireless sensor nodes in a real clinical environment.

V. Conclusion

This article detailed the design and testing of a 6-DOF wireless sensor node with submillimeter and subdegree tracking accuracy with immediate applications in image-guided cardiothoracic procedures. The sensor node presented here has a 3 cm diameter and is designed to perform as a patient registration and motion compensation reference. The wireless sensor node enhances the usability of the open-source Anser EMT system by removing the reliance on a wired connection from the sensor to the control unit. The phase synchronization technique outlined in this article solves the loss-of-phase problem associated with wireless sensor sampling networks. The wireless tracking system was demonstrated in a realistic breathing lung simulator and proved capable of measuring breathing motion in real time with a 25-Hz update rate.

Future work will include further power optimization and device miniaturization, directly solving sensor pose on the wireless nodes and compatibility with commercially available EMT systems.

Acknowledgment

Open Access funding was provided by the IReL Consortium. Views and opinions expressed are, however, those of the author(s) only and do not necessarily reflect those of the European Union or the European Research Council. Neither the European Union nor the granting authority can be held responsible for them.

References

[1] A. M. Franz, T. Haidegger, W. Birkfellner, K. Cleary, T. M. Peters, and L. Maier-Hein, "Electromagnetic tracking in medicine—A review of technology, validation, and applications," *IEEE Trans. Med. Imag.*, vol. 33, no. 8, pp. 1702–1725, Aug. 2014.

[2] J. Hummel et al., "Evaluation of a new electromagnetic tracking system using a standardized assessment protocol," *Phys. Med. Biol.*, vol. 51, no. 10, pp. N205–N210, Apr. 2006.

[3] Z. Yaniv, E. Wilson, D. Lindisch, and K. Cleary, "Electromagnetic tracking in the clinical environment," *Med. Phys.*, vol. 36, no. 3, pp. 876–892, Mar. 2009.

[4] C. Piorkowski and G. Hindricks, "Nonfluoroscopic sensor-guided navigation of intracardiac electrophysiology catheters within prerecorded cine loops," *Circulat., Arrhythmia Electrophysiology*, vol. 4, no. 4, pp. 36–38, Aug. 2011.

[5] H. A. Jaeger et al., "Peripheral tumour targeting using open-source virtual bronchoscopy with electromagnetic tracking: A multi-user preclinical study," *Minimally Invasive Therapy Allied Technol.*, vol. 28, no. 6, pp. 363–372, Nov. 2019.

[6] A. C. Mehta, K. L. Hood, Y. Schwarz, and S. B. Solomon, "The evolutional history of electromagnetic navigation bronchoscopy: State of the art," *Chest*, vol. 154, no. 4, pp. 935–947, Oct. 2018.

[7] M. Feuerstein, T. Sugiura, D. Deguchi, T. Reichl, T. Kitasaka, and K. Mori, "Marker-free registration for electromagnetic navigation bronchoscopy under respiratory motion," in *Medical Imaging and Augmented Reality*. Berlin, Heidelberg: Springer, 2010, pp. 237–246.

[8] Y.-H. Kim et al., "2019 APHRS expert consensus statement on three-dimensional mapping systems for tachycardia developed in collaboration with HRS, EHRA, and LAHRS," *J. Arrhythmia*, vol. 36, no. 2, pp. 215–270, Mar. 2020.

[9] D. Bhakta and J. M. Miller, "Principles of electroanatomic mapping," *Indian Pacing Electrophysiology J.*, vol. 8, no. 1, pp. 32–50, Feb. 2008.

[10] L. Gepstein and S. J. Evans, "Electroanatomical mapping of the heart: Basic concepts and implications for the treatment of cardiac arrhythmias," *Pacing Clin. Electrophysiology*, vol. 21, no. 6, pp. 1268–1278, Jun. 1998.

[11] H. A. Jaeger et al., "Anser EMT: The first open-source electromagnetic tracking platform for image-guided interventions," *Int. J. Comput. Assist. Radiol. Surgery*, vol. 12, no. 6, pp. 1059–1067, Jun. 2017.

[12] J. J. Moré, "The Levenberg–Marquardt algorithm: Implementation and theory," in *Numerical Analysis* (Lecture Notes in Mathematics), vol. 630. Berlin, Germany: Springer, 1978, pp. 105–116.

[13] M. Cavaliere, D. Crowley, H. A. Jaeger, K. O'Donoghue, and P. Cantillon-Murphy, "Magnetic model calibration and distortion compensation for electromagnetic tracking in a clinical environment," *IEEE Trans. Magn.*, vol. 59, no. 7, pp. 1–12, Jul. 2023.

[14] H. Park, C. Park, S.-J. Kweon, J.-H. Suh, J. Choi, and M. Je, "Miniature electromagnetic sensor nodes for wireless surgical navigation systems," in *Proc. IEEE Int. Symp. Circuits Syst. (ISCAS)*, Seville, Spain, Oct. 2020, pp. 1–5, doi: 10.1109/ISCAS45731.2020.9180508.

[15] M. Monge, A. Lee-Gosselin, M. G. Shapiro, and A. Emami, "Localization of microscale devices in vivo using addressable transmitters operated as magnetic spins," *Nature Biomed. Eng.*, vol. 1, no. 9, pp. 736–744, Sep. 2017.

[16] S. Sharma et al., "Wireless 3D surgical navigation and tracking system with 100μm accuracy using magnetic-field gradient-based localization," *IEEE Trans. Med. Imag.*, vol. 40, no. 8, pp. 2066–2079, Aug. 2021.

[17] J. Jang et al., "A four-camera VGA-resolution capsule endoscope system with 80-Mb/s body channel communication transceiver and sub-centimeter range capsule localization," *IEEE J. Solid-State Circuits*, vol. 54, no. 2, pp. 538–549, Feb. 2019.

[18] M. Rustom and C. Sideris, "Design and implementation of a low power wireless frequency-division multiplexed magnetic 3D localization scheme with sub-mm precision for capsule endoscopy applications," *IEEE Solid-State Circuits Lett.*, vol. 6, pp. 37–40, 2023.

[19] A. Ray, I. Habibagahi, and A. Babakhani, "A fully wireless and batteryless localization system with 50 micrometre motion detection capability and adaptive transmitter power control for point-of-care biomedical applications," *IEEE Trans. Biomed. Circuits Syst.*, vol. 17, no. 4, pp. 1–14, Aug. 2023.

[20] D. Crowley, M. Cavaliere, and P. Cantillon-Murphy, "A novel approach to wireless electromagnetic tracking using frequency modulation radio communication," *Int. J. Comput. Assist. Radiol. Surgery*, vol. 18, no. 9, pp. 1707–1713, Jun. 2023.

[21] C. Pande and P. Cantillon-Murphy, "System framework for Bluetooth-based wireless electromagnetic tracking and navigation system," in *Proc. IEEE EMBS Int. Conf. Biomed. Health Informat.*, Oct. 2022, pp. 1–12.

[22] M. Cavaliere, O. McVeigh, H. A. Jaeger, S. Hinds, K. O'Donoghue, and P. Cantillon-Murphy, "Inductive sensor design for electromagnetic tracking in image guided interventions," *IEEE Sensors J.*, vol. 20, no. 15, pp. 8623–8630, Aug. 2020.

[23] C. Pande, H. Jaeger, K. O'Donoghue, and P. Cantillon-Murphy, "Bluetooth-based wireless electromagnetic tracking and navigation system," in *Proc. IEEE EMBS Int. Conf. Biomed. Health Informat.*, Jul. 2021, pp. 1–29.

[24] B. K. P. Horn, "Closed-form solution of absolute orientation using unit quaternions," *J. Opt. Soc. Amer. A, Opt. Image Sci.*, vol. 4, no. 4, p. 629, Apr. 1987.

[25] K. O'Donoghue et al., "Evaluation of a novel tracking system in a breathing lung model," in *Proc. 36th Annu. Int. Conf. IEEE Eng. Med. Biol. Soc.*, Aug. 2014, pp. 4046–4049.

[26] A. Fedorov et al., "3D slicer as an image computing platform for the quantitative imaging network," *Magn. Reson. Imag.*, vol. 30, no. 9, pp. 1323–1341, Nov. 2012.

[27] M. Srivastava et al., "3D position tracking using on-chip magnetic sensing in image-guided navigation bronchoscopy," *IEEE Trans. Biomed. Circuits Syst.*, vol. 1, no. 1, pp. 1–17, Jun. 2024.

[28] R. A. MacLachlan, R. L. Hollis, B. Jaramaz, C. N. Riviere, J. N. Martel, and K. L. Urish, "Multirate Kalman filter rejects impulse noise in frequency-domain-multiplexed tracker measurements," in *Proc. IEEE Sensors*, Oct. 2017, pp. 1–3.

[29] X. Luo et al., "Evolutionarily optimized electromagnetic sensor measurements for robust surgical navigation," *IEEE Sensors J.*, vol. 19, no. 22, pp. 10859–10868, Nov. 2019.

[30] A. Chen, N. Pastis, B. Furukawa, and G. A. Silvestri, "The effect of respiratory motion on pulmonary nodule location during electromagnetic navigation bronchoscopy," *Chest*, vol. 147, no. 5, pp. 1275–1281, May 2015.

[31] J. Borgert et al., "Respiratory motion compensation with tracked internal and external sensors during CT-guided procedures," *Comput. Aided Surgery*, vol. 11, no. 3, pp. 119–125, Jan. 2006.

Daragh Crowley (Member, IEEE) received the B.E. (Hons.) degree in electrical and electronic engineering from University College Cork (UCC), Cork, Ireland, in 2021, where he is currently pursuing the Ph.D. degree in electrical and electronic engineering with the Tyndall National Institute.

In 2024, he worked with the Sheikh Zayed Institute for Pediatric Surgical Innovation, Children's National Hospital, Washington, DC, USA. His current research interests include image-guided surgical navigation, electromagnetic tracking, and wireless embedded systems.

Marco Cavaliere (Member, IEEE) received the Laurea Magistrale degree in electrical energy engineering from the University of Padua, Padua, Italy, in 2019, and the Ph.D. degree in electrical and electronic engineering from University College Cork, Cork, Ireland, in 2023.

Dr. Cavaliere's research interests include real-time locating systems (RTLS), radar systems, ultra-wide band (UWB) technology, and electromagnetic tracking and navigation for image-guided interventions.

Eoin Higgins (Member, IEEE) received the B.Sc. degree in applied physics from Eindhoven University of Technology, Eindhoven, The Netherlands, in 2022. He is currently pursuing the Ph.D. degree in electrical and electronic engineering with the Tyndall National Institute, University College Cork, Cork, Ireland.

His current research interests include electromagnetic tracking and navigation systems for image-guided interventions.

Charu Pande (Member, IEEE) received the M.S. degree in electrical and electronic engineering from the University of Texas at Arlington, Arlington, TX, USA, in 2015.

She was a Research Scholar with the Tyndall National Institute, University College Cork, Cork, Ireland, from 2019 to 2023.

Herman Alexander Jaeger (Member, IEEE) received the B.E., M.Eng.Sc., and Ph.D. degrees from University College Cork (UCC), Cork, Ireland, in 2014, 2015, and 2018, respectively.

In 2015, he worked with the Hamlyn Institute for Robotic Surgery, Imperial College London, London, U.K., developing novel camera tracking algorithms for minimally invasive surgery. From 2016 to 2017, he was a Visiting Researcher with the Institute for Image Guided Surgery (IHU), Strasbourg, France, where he developed Anser electromagnetic tracking (EMT), the world's first open-source magnetic tracking system for guided surgical interventions. From 2019 to 2022, he worked as a Postdoctoral Researcher with the Tyndall National Institute, UCC, where he worked on novel magnetic sensors for surgical navigation. In 2022, he joined the School of Engineering, UCC, as a Lecturer of Electrical and Electronic Engineering, where he teaches courses in power systems and biomedical electronics. His current research interests include EMT for virtual reality (VR)/augmented reality (AR) applications.

Kilian O'Donoghue received the B.E. and Ph.D. degrees in electrical and electronic engineering from University College Cork, Cork, Ireland, in 2011 and 2015, respectively.

He has over 12 years of experience in medical electronic design and has worked in multiple start-up and early stage medical device companies in Ireland and Canada, developing core technologies in robotics, sensing, navigation, and medical imaging systems. He is also the CEO and the Co-Founder of Quadrant Scientific Ltd., Cork, a company specializing in cutting-edge electromagnetic navigation technology. His research interests include electromagnetic (EM) tracking systems, circuit design, magnetic field modeling, and minimally invasive surgeries.

Pádraig Cantillon-Murphy (Senior Member, IEEE) received the B.E. (Hons.) degree in electrical and electronic engineering from University College Cork (UCC), Cork, Ireland, in 2003, and the Master of Science and Ph.D. degrees from the Department of Electrical Engineering and Computer Science, Massachusetts Institute of Technology (MIT), Cambridge, MA, USA, in 2005 and 2008, respectively.

He is a Professor of Biomedical Engineering with UCC, where he is also an Academic Member of the Tyndall National Institute, and an Honorary Faculty with the l'Institut de Chirurgie Guidée par l'Image, Strasbourg, France. He has co-founded two start-up companies. His current research interests include electromagnetic tracking and navigation in image-guided interventions, and surgical robotics. His teaching interests include electronic circuits, electromagnetics, and biomedical design.

Dr. Cantillon-Murphy was a former Marie Curie Fellow from 2010 to 2014, a former MIT Whitaker Fellow from 2007 to 2008, and an ERC Awardee in 2020.